



Parameter optimization and mechanical properties of 42CrMo4 manufactured by laser powder bed fusion

Chuan Shi¹ · Stefan Dietrich¹ · Volker Schulze¹

Received: 10 February 2022 / Accepted: 30 May 2022 / Published online: 4 June 2022
© The Author(s) 2022

Abstract

To study the manufacturability and mechanical properties of a low alloy heat treatable medium carbon steel by additive manufacturing, 42CrMo4 (AISI4140) specimens were manufactured by laser powder bed fusion. Influences of processing parameters on relative density and crack density were investigated. Moreover, Charpy impact tests, microhardness, and tensile tests for specimens with and without preheating were also studied. Results showed that the primary defects in the microstructure of additively manufactured samples were the lack of fusion pores and microcracks. The variation of processing parameters influences the porosity and microcracks prominently. The impact toughness of specimens with preheating is around three times higher than specimens without preheating. However, post heat treatment for as-built specimens, such as tempering at different temperature ranges, did not improve the impact toughness further. The detailed fracture mechanism for the massive difference in the impact toughness was investigated.

Keywords Laser powder bed fusion · Quench and tempering steel · Processing parameters optimization · Charpy impact test

1 Introduction

Laser powder bed fusion (LPBF), or selective laser melting (SLM), is the most prominent additive manufacturing (AM) technology to manufacture near-net-shape metal components. It has the advantage of the high complexity of parts, relatively low material waste, and high flexibility of parameter control during laser melting of the powder. Moreover, LPBF is suitable for an extensive range of metals, for example, stainless steel, aluminum alloys, nickel alloys, and titanium alloys [1]. However, manufacturing carbon steel, especially with medium or high contents of carbon, is still a challenging task at the moment because of severe defects in microstructure [2, 3], such as (a) microcracks due to high thermal stress and martensitic transformation and (b) lack of fusion pores (LoF), which can be ascribed to poor weldability and the severe balling effect caused by Rayleigh instability [4]. Consequently, all these issues indicate a

narrow processing window for this kind of medium or high carbon steel by LPBF.

AISI 4140 (German grade 42CrMo4) is such a kind of low alloy medium carbon steel. It is generally manufactured in quenching and tempering (Q&T) states to get sufficient strength and retain appropriate toughness to be applied as structural components in automotive, aircraft, and oil industries, such as gears and shafts couplings. Wang et al. [5] studied the processing parameter window and mechanical properties of AISI 4140 specimens fabricated by LPBF. It is found that the strength and toughness of specimens were improved compared with conventionally manufactured counterparts. However, they just showed the feasibility and promising mechanical results of additive manufacturing AISI 4140. More information about the detailed microstructure analysis or fractured surface information is unavailable. Damon et al. [3] reported AISI 4140 samples manufactured by laser powder bed fusion at 200 °C base-plate temperature, and their results showed that samples with higher densities (over 99.5%) could be achieved by adjusting processing parameters. Although pores could be reduced by optimizing parameters, microcracks still occurred even with base preheating, and the existence of microcracks may have a detrimental impact on mechanical properties. Jelis et al.

✉ Chuan Shi
chuan.shi@kit.edu

¹ Institute for Applied Materials (IAM-WK), Karlsruhe Institute of Technology (KIT), Engelbert-Arnold-Straße 4, 76131 Karlsruhe, Germany

[6] researched AISI 4340 steels manufactured by LPBF, and they pointed out that the volumetric energy density for fabricating fully dense parts is around 141.7 J/mm^3 , and the presence of oxygen in the chamber has a negative effect on strength. Still, cracks were observed. Literature [7–10] for other medium even high carbon-bearing steels processed by LPBF suggested that post-treatment like hot isostatic pressuring (HIP) is an efficient method to reduce pores and microcracks in the microstructure, but it may also cause grain coarsening in the meantime. Although preheating is the most used method to reduce thermal stresses by decreasing the temperature gradient in the LPBF process and thereby reducing cracking susceptibility, the input energy of the laser must also be chosen appropriately. This raises the question of whether it is possible to reduce or even eliminate defects, especially microcracks in AISI 4140 parts manufactured by LPBF, just by optimizing the processing parameters, for instance, by adjusting scanning speed, power, hatching distance, and layer thickness and shifting the angle of each layer. The focus should be put on this point because the unique advantage of LPBF technology is the near-net-shape ability with good mechanical properties. Additional post-treatment will drastically increase the overall manufacturing cost in terms of time or finance. However, information on fabricating such process-microstructure-property correlations for LPBF AISI 4140 is rare.

Strength and toughness are two of the essential mechanical properties of structural materials, and it is meaningful only if the mechanical properties of LPBF parts are comparable to or better than conventionally manufactured parts. The most used method for evaluating toughness is the dynamic Charpy impact test which generally uses upper shelf energy (USE) as fracture resistance values [11]. Published literature [11–16] shows that crystallographic textures, grain size, chemical composition, and heat treatment methods significantly affect the Charpy impact toughness of metals manufactured by the conventional method. Only a few works of metal materials manufactured by LPBF reported Charpy impact tests in detail. Wang et al. [17] compared the Charpy toughness of forged annealing 30CrMnSiA samples with LPBF counterparts, and results showed that LPBF parts have lower impact energy than the conventionally manufactured ones, and they ascribed the reason to stress concentration and carbides segregation. Huang et al. [18] reported the anisotropic toughness of China low activation martensitic (CLAM) steel manufactured by LPBF, and it was found that the anisotropy in microstructure and the orientation of defects in the interface of layers were the main reason for anisotropic toughness. Normally tensile strength of LPBF steel parts can be improved or comparable to when compared with conventionally fabricated ones, which may result from the quick solidification with a formation of finer grains. Another reason may be attributed to the formation

of metastable martensite with higher strength in microstructure, which can also reduce toughness due to the brittleness of martensite.

Although defects such as LoF pores and cracking in the specimen manufactured by LPBF are thought detrimental to mechanical performance, the influence of different porosity levels on the extent of mechanical performance degradation is still not so clear. Moreover, the influence of manufacturing size on defects with and without preheating should be further investigated. To the best of the authors' knowledge, there are few reports regarding that aspect in LPBF 42CrMo4.

This work aims to develop a comprehensive understanding of the influence of processing parameters on porosity and cracking in as-built status. Furthermore, the investigation of the influences of defects on the mechanical properties, like Charpy impact toughness and tensile strength, and the comparison of mechanical properties with conventionally fabricated counterparts, with and without preheating conditions, is helpful to the exploration of LPBF AISI4140 steel with a good combination of strength and toughness for future application in innovative structures.

2 Materials and experiments

2.1 Materials

The powder used in this paper was produced by gas atomization by Höganäs, as shown in Fig. 1. The chemical composition of the powder is shown in Table 1. The average powder diameter is $22 \mu\text{m}$, d_{10} is $14.02 \mu\text{m}$, d_{50} is $20.92 \mu\text{m}$, and d_{90} is $28.42 \mu\text{m}$.

2.2 Specimens preparation

All samples were fabricated in an ORLASER CREATOR machine equipped with a 250 W Yb: fiber laser source (Fig. 2), and the wavelength was 1070 nm. The manufacturing process was conducted in an Argon gas environment (oxygen content in the chamber was maintained at around 0.01% to avoid possible oxidation).

Processing parameters were optimized by fabricating $\phi 10 \times 10 \text{ mm}$ cylindrical samples via relative density and microcracks density. The optimized parameters chosen from processing maps (Fig. 3) were further used to manufacture specimens for mechanical tests. For Charpy tests, samples were manufactured in dimensions of $15 \times 15 \times 60 \text{ mm}$ and machined to $10 \times 10 \times 55 \text{ mm}$, following the standard described in ASTM E23-18. The building direction of specimens was perpendicular to the build platform. For uniaxial tensile tests, specimens were built in the size of $\phi 10 \times 60 \text{ mm}$. Then dog-bone-shaped samples were

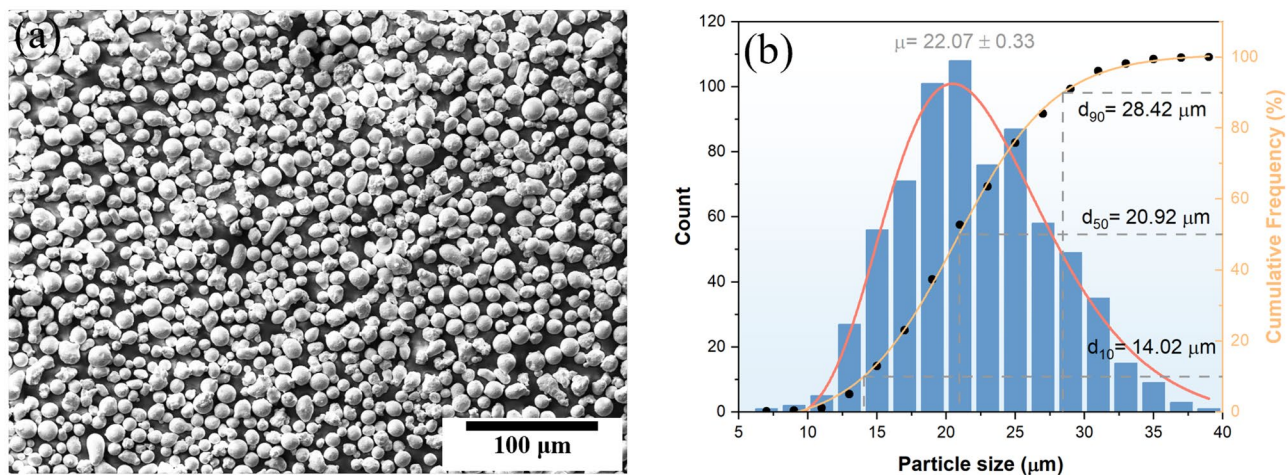


Fig. 1 (a) SEM image of 42CrMo4 powder used for the LPBF and (b) the particle size distribution. μ is the mean value of powder size

machined with a gauge diameter of 5 mm and a gauge length of 30 mm according to DIN 50,125.

In order to make comparisons, a number of specimens were fabricated by preheating the build platform at 200 °C during the whole manufacturing process (marked as P+AB), and others were not (marked as AB). Additionally, some as-fabricated specimens were further tempered at 450 °C and 600 °C for 2 h, respectively, and then cooled down at ambient air (marked as AB+T450 and AB+T600 separately).

2.3 Experiments and characterization

The relative density of specimens was measured according to Archimedes’ principle using a precision balance ME503TE, and distilled water was used as the medium for the measurement. Relative density is equal to $\left(\frac{\rho_{measured}}{\rho_{ref}}\right) \times 100\%$ and $\rho_{ref} = 7.83 \text{ g/cm}^3$. Three specimens for each parameter were measured to get the average relative density value. The crack density was measured by the image threshold technics via ImageJ software by measuring the length of each crack in metallographic sections. Then, the total lengths of cracks were divided by the total areas measured in images to get the crack density (mm/mm^2). Processing maps were plotted using the 2D heatmap function in the Originlab software, and each small block in the heatmap represents one set of processing parameter data in our experiments. Additionally, all original data for relative density and crack density measurement can be found in Supplementary Tables S1 and S2.

The Charpy impact test was conducted using a Frank Pendulum at room temperature. Five pieces for each parameter group were tested, and values of test results were averaged in this work. Microhardness of specimens was measured by using a Qness Q10A Vickers digital microhardness tester with a load of 100 g and a dwell time of 10 s. The tensile tests were conducted using a Zwick/Roell 1484 (200 KN) tester with a strain rate of 0.001 /s at room temperature. The processing parameter and heat treatment conditions of specimens for Charpy and tensile tests can be seen in Supplementary Table S3.

Specimens for microstructural characterization were cut, embedded, mechanically ground, and polished. The microstructure characteristics and fracture surfaces were analyzed by a Leitz Aristomet optical microscope and Zeiss Leo50 scanning electron microscope (SEM) at an accelerating voltage of 20 kV.

3 Results

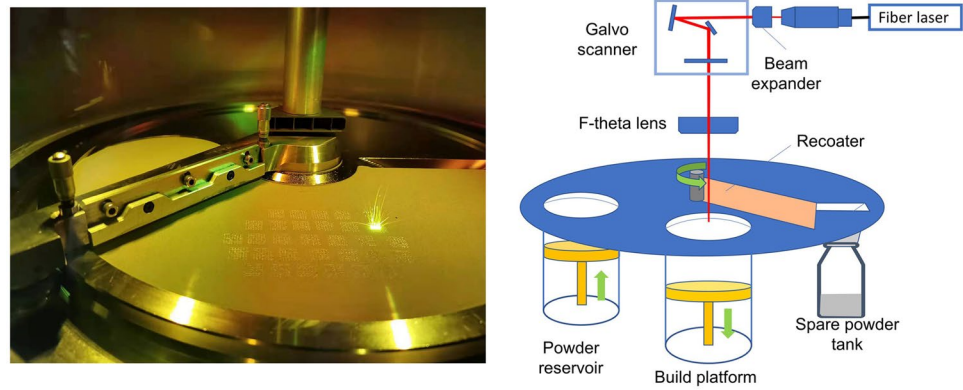
3.1 Processing parameters optimization

Figure 3 shows the results of the relative density for different processing parameters. It can be found that (Fig. 3a–c) the relative density is the lowest when selecting the lowest laser power (175 W) and the highest scanning speed (1500 mm/s) simultaneously. When the laser power is 250 W, the scanning speed is 1300 mm/s, and the hatching distance is 60 μm, the highest relative density, over 99%,

Table 1 Chemical composition of the powder particles in wt %

Element	C	Cr	Mo	Mn	Si	P	S	Fe
	0.39	1.0	0.2	0.9	0.4	0.026	0.006	Bal

Fig. 2 Schematic diagram of laser powder bed fusion



was obtained. It can also be found in Fig. 3b when the processing parameter is 200 W/500 mm/s, the relative density of the specimen (around 98.57%) is close to the relative density of 250 W/1300 mm/s. The reason can be explained

that when the scanning speed is 500 mm/s, the main defect in the microstructure is cracking, and few large LoF pores or keyhole pores could be found (Supplementary Fig. S1). However, the relative density dropped to 97.86% when

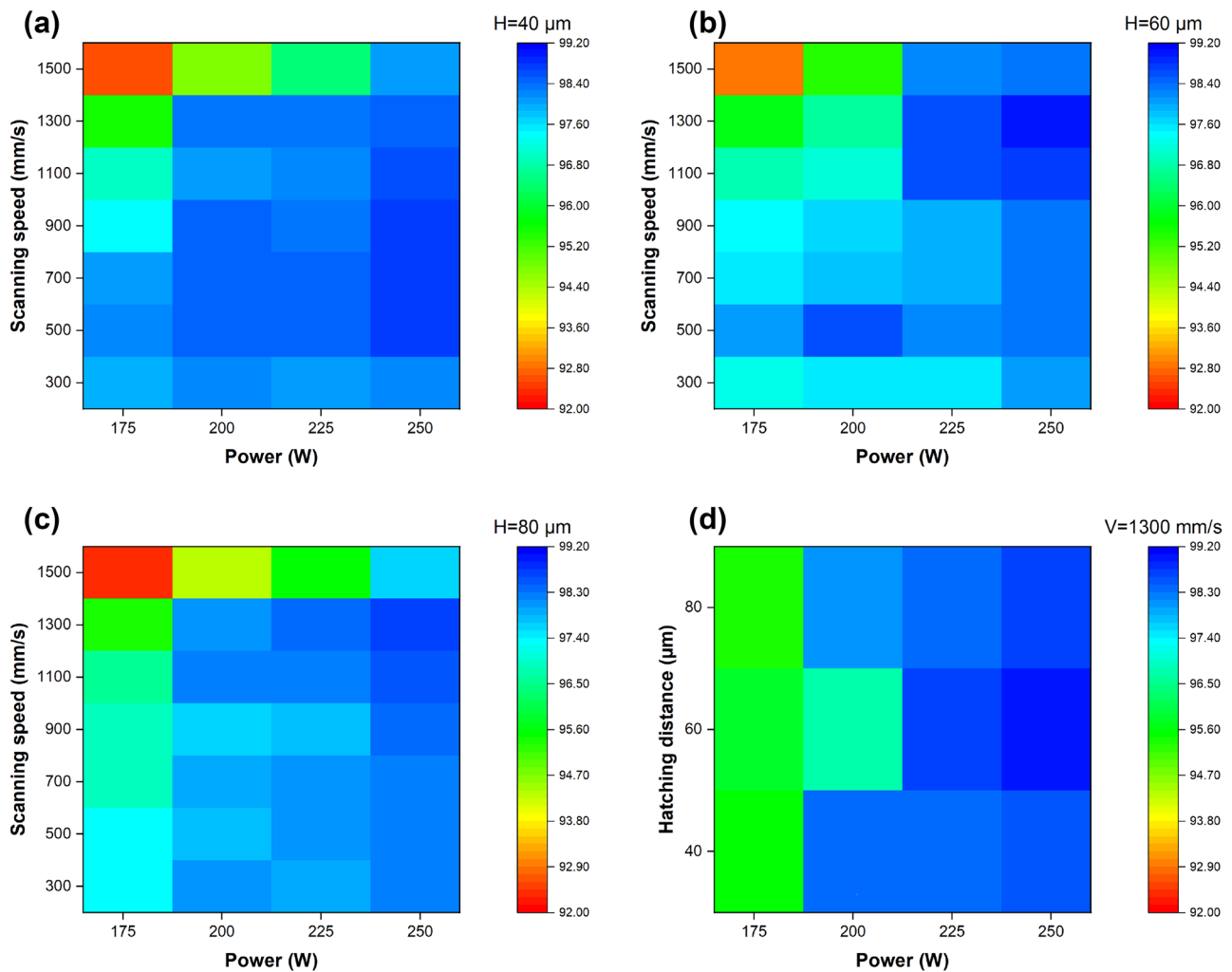


Fig. 3 Variation of relative density of specimens manufactured with different processing parameters; (a) $H=40\ \mu\text{m}$, (b) $H=60\ \mu\text{m}$, and (c) $H=80\ \mu\text{m}$. (d) The relationship between laser power and hatching distance on the relative density, $V=1300\ \text{mm/s}$

the laser scanning speed increased to 700 mm/s due to the occurrence of LoF pores. It is also interesting to note that laser power has a more prominent influence on the relative density than hatching distance. Namely, the density is improved prominently with increasing the power (Figs. 3d and 4).

Apart from relative density, cracks are another factor that should be considered in the LPBF of 42CrMo4, which generally originate from a steep temperature gradient. Figure 5 shows the variation trend of pores and cracks with different scanning speeds. The most significant variation is that the crack density sharply reduced from 3.01 to 0.23 mm/mm² with increasing scanning speed from 300 to 1500 mm/s, and this trend can be seen clearly in the overall crack density map (Fig. 6). Moreover, the crack density trend also indicates that specimens with low crack density can be obtained by choosing either low or high power but with a fast scanning speed (over 900 mm/s). Besides, pores vary from small spherical keyhole pores ($V = 300$ mm/s) to large lack of fusion pores ($V = 900$ mm/s) and then to small spherical pores again ($V = 1300$ – 1500 mm/s) when scanning speed is varied from 300 to 1500 mm/s. It is also interesting to note in Fig. 6 that when the scanning speed ranges from 500 to 1100 mm/s, the crack density of specimens at a laser power

of 200 W is higher than 175 W. The possible reason could be that there are more LoF pores when the laser power is 175 W than at a laser power of 200 W with the same level of scanning speed, and cracking is easy to form on the boundaries of irregular LoF pores due to stress concentration.

The optimized processing parameters chosen to fabricate specimens for further studies were combined with low crack density and high relative density: laser power 250 W, scanning speed 1300 mm/s, hatching distance 60 μ m, powder layer thickness 30 μ m, and scan rotation between successive layers is 67°.

3.2 Charpy impact tests

Results in Fig. 7 show the impact energy of specimens under various conditions. For LPBF specimens, the specimen manufactured with preheating has the highest impact energy (20.75 J), which is 3–4 times higher than other LPBF samples (4.79–5.69 J). Moreover, a comparison of the as-built specimen and specimens with post heat treatment shows that further tempering process for as-fabricated specimens cannot effectively improve the impact energy but even decrease slightly. It is also worth noting that although all LPBF specimens were fabricated with the optimized

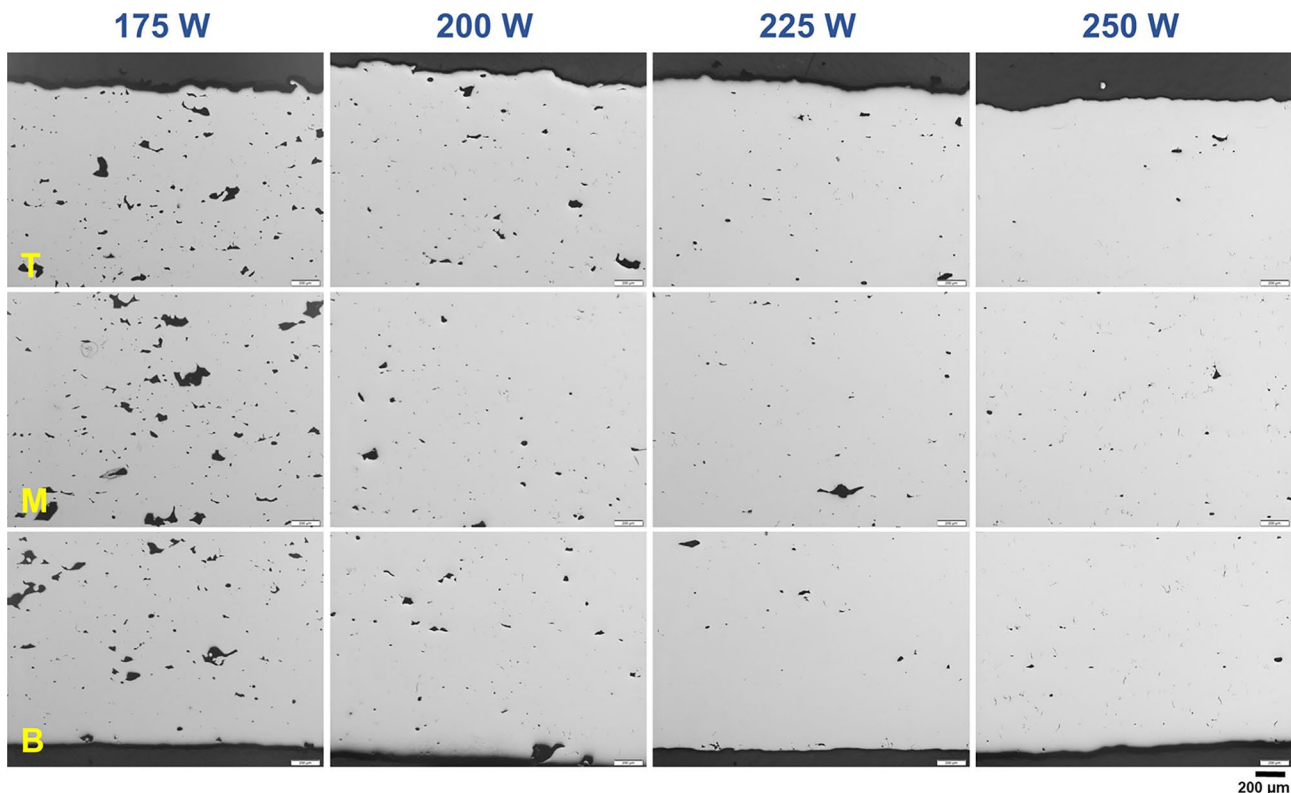


Fig. 4 Optical microscope images of LPBF specimens manufactured with the laser power ranging from 175 to 250 W, $V = 1300$ mm/s, and $H = 60$ μ m. T represents the top of the specimen, M represents the middle part, and B represents the bottom

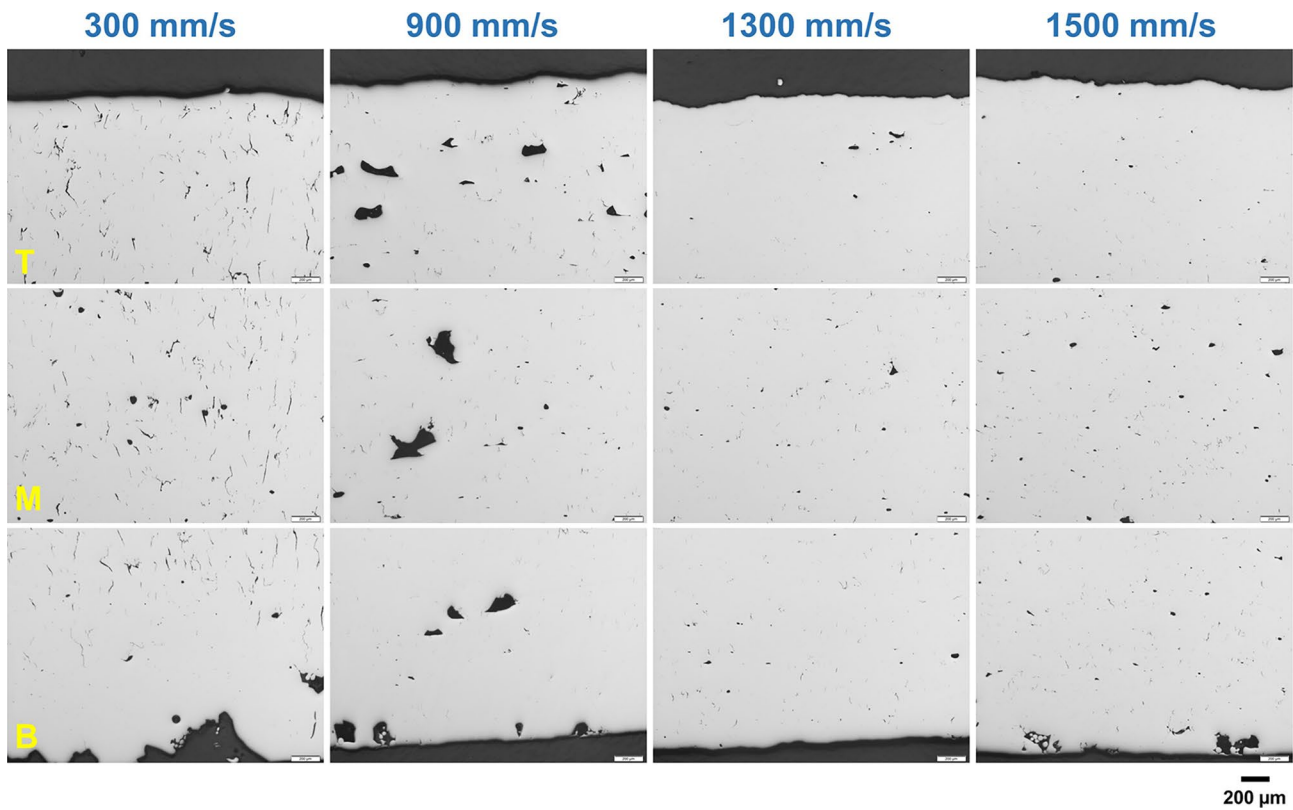


Fig. 5 Optical figures of the LPBF specimens manufactured with the laser scanning speed ranging from 300 to 1500 mm/s. P=250 W, H=60 μ m. T represents the top of the specimen, M represents the middle part, and B represents the bottom

parameters as described aforementioned, the relative density of larger Charpy test samples decreases from over 99 to 97.7%. Nonetheless, the relative density of the specimen manufactured with preheating treatment seems not to fluctuate much (99.4%), and the high relative density may be one of the essential reasons why P+AB samples have higher

impact energy in the Charpy impact tests than others. The influence of manufacturing size on pores, cracking, and microhardness will be discussed in the “Influence of manufacturing size on defects”.

The diagram of hardness in Fig. 7b suggests that the AB specimen has the highest value (504.98 HV_{0.1}), while P+AB and AB+T450 specimens have similar microhardness values. It indicates that preheating at 200 °C in LPBF has a similar function as tempering at 450 °C for post-treatment to adjust the microhardness. Although the value for AB+T600 is the lowest (352.53 HV_{0.1}), it does not help improve the impact toughness, indicating hardness is not the most important factor affecting the impact toughness.

3.3 Tensile tests

The overall mechanical properties are concluded in Table 2. The P+AB specimen has the highest average tensile strength (1359 MPa), and it is around 100 MPa higher than that without preheating (AB₂₅₀), suggesting that base preheating is beneficial to improving tensile strength. The AB₁₇₅ specimen has the lowest tensile strength (822.4 MPa), only about 65% of that of the AB₂₅₀ specimen. Moreover, the elongation at fracture of the AB₁₇₅ specimen is only about 0.1%, indicating

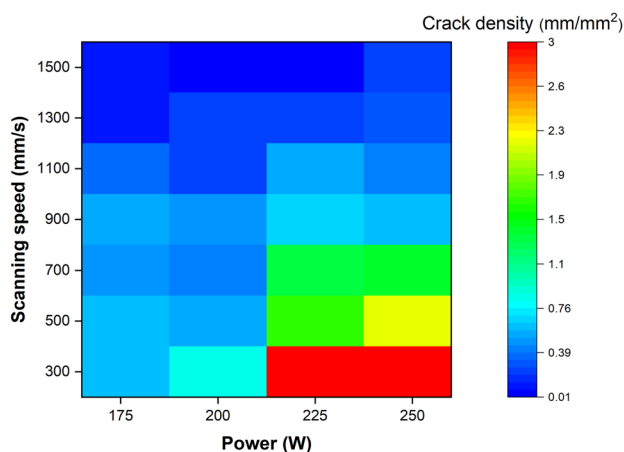


Fig. 6 Variation of the crack density of the LPBF specimens fabricated with different processing parameters. H=60 μ m

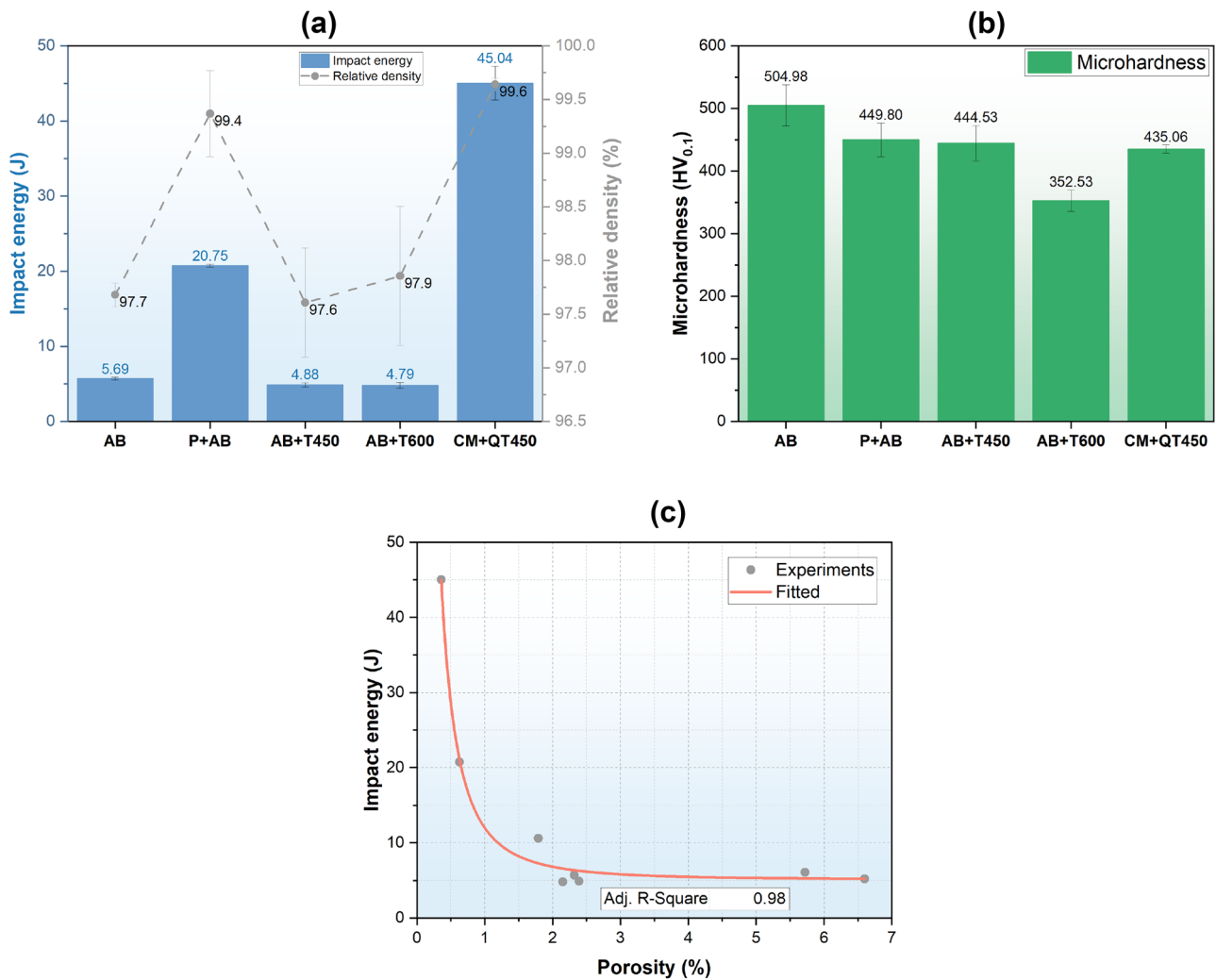


Fig. 7 (a) The impact energy and relative density of samples with different manufacturing or post-treating conditions, (b) the responding microhardness of Charpy impact tests specimens, and (c) the relationship between porosity and the impact energy

the severe brittle fracture of AB specimens fabricated with low power. Although the value of UTS of the P+ AB specimen is comparable to that from literature, the elongation at fracture (2.12%) is only approximate 17.2–29.4%.

4 Discussion

4.1 Influence of processing parameters on defects

Lack of fusion pores and hot cracks are two primary defects in the LPBF of 42CrMo4 material. LoF pores are usually caused by insufficient input energy to melt the powder and consolidate the track on the previous layer, and hot cracks are caused by the tensile residual stress, which generally originates from a steep temperature gradient during the rapid melting and solidifying process [19, 20].

4.1.1 Laser power

Laser power affects LoF pores directly, and a continuous and stable melted track can be guaranteed with high laser power. However, high laser power can lead to keyhole problems, which is the reason for some large spherical pores in the 250 W-1300 mm/s specimen, and it also agrees with results reported by Anton [21]. In contrast, low laser power (<200 W) cannot fully melt through the powder layer and will cause severe LoF defects.

4.1.2 Laser scanning speed

Laser scanning speed affects pore formation by affecting the time; the laser and powder are in contact. Fast scanning speed indicates less contact time between laser and powder than the low scanning speed, and it may cause small melt

Table 2 Mechanical properties of the LPBF specimens

Specimens	Relative density (%)	Crack density (mm/mm ²)	Impact energy (J)	UTS (MPa)	YS _{0.2%} (MPa)	A _f (%)	Hardness (HV _{0.1})
C-AB	97.7 ± 0.11	0.37 ± 0.03	5.69 ± 0.20	-	-	-	505 ± 33.1
C-P + AB	99.4 ± 0.40	< 0.01	20.75 ± 0.19	-	-	-	450 ± 27
C-AB + T450	97.6 ± 0.51	0.42 ± 0.05	4.88 ± 0.27	-	-	-	445 ± 28.3
C-AB + T600	97.9 ± 0.65	0.38 ± 0.03	4.79 ± 0.41	-	-	-	353 ± 17
C-CM + QT450	99.6 ± 0.06	0	45.04 ± 2.23	-	-	-	435 ± 6.6
T-AB ₁₇₅	94.6 ± 0.46	0.17 ± 0.06	-	822.4 ± 122	-	0.1	560 ± 30.4
T-AB ₂₅₀	98.2 ± 0.32	0.33 ± 0.04	-	1259.8 ± 11	1147.6 ± 37.1	1.15 ± 0.3	508 ± 25.1
T-P + AB ₂₅₀	99.4 ± 0.17	< 0.01	-	1359 ± 14	1267.3 ± 10.4	2.12	439 ± 24.5
Damon et al. [3]	~99.5	-	-	1280 ± 10	1175 ± 5	7.2 ± 2.8	~390
Wang et al. [5]	-	-	32.1	1446.5	1289	12.3	~440

C Charpy impact test, T tensile test

pools to be unstable during the manufacturing process compared to low scanning speeds because of Plateau-Rayleigh instability [22]. Accordingly, LoF pores occur because of too high scanning speed, especially with low laser power. Although low scanning speed is beneficial for the contact between laser and powder, it still may raise intense spattering and turbulent evaporation in the melt pool and hence cause severe keyholes during the process [23], which can be the reason for keyhole pores observed in the microstructure with low laser scanning speed (Fig. 5; 300 mm/s).

4.1.3 Hatching distance

Hatching distance is another significant parameter as too large hatching values may cause the neighboring tracks not to bond well and generate LoF pores. Also, too small values may lead to overheating of the former layers, thereby inducing severe hot cracking [24, 25].

4.1.4 Volumetric energy density

Altogether, the parameter optimization process aims at finding a set of parameters, including power, scanning speed, hatching distance, and layer thickness, to get the highest density and the lowest crack density. Literature [26–28] shows that volumetric energy density (VED) is an excellent method to take all necessary parameters into consideration, which can be described using the equation as follows:

$$VED = \frac{P}{V \cdot H \cdot t} \quad (1)$$

where P is laser power, V is scanning speed, t is layer thickness of powder, and H is hatching distance. The volumetric energy density of the optimized parameters in this experiment is around 106.8 J/mm³, and it is similar to the value of

80–100 J/mm³ provided by other researchers studying LPBF 42CrMo4 [3, 5].

Nevertheless, the relative density of samples from experiments could still be very low even with a similar volumetric energy density, like in the vicinity of 100 J/mm³, the lowest value is even close to 92% (see Fig. 8a). It suggests that laser power may be the most suitable reference to obtain high relative density rather than volumetric energy density. Moreover, the near-linear relationship between energy density and crack density shows that cracks are susceptible to high energy density. Especially when the energy density is over 400 J/mm³, the crack density is even about 3 mm/mm². High energy density means high energy input per cubic millimeter, and it can cause a considerable temperature gradient and residual stress during the layer upon layer process because of the rapidly melting and solidifying. In the meantime, the expansion of martensite transformation will also increase cracking, making the material more sensitive to cracking [29]. Additionally, the lack of base preheating could also deteriorate the cracking susceptibility due to the large temperature gradient.

It should be noted that the VED can also be affected by the layer thickness with different particle size distributions. When the powder particle size is over the layer thickness (30 μm in this paper), it will potentially increase the layer thickness and decrease the VED, according to Eq. (1). Meanwhile, the powder with large size will also leave large voids between each other when without sufficient small particles to complement, finally inducing LoF pores. However, the d_{50} and d_{90} of 42CrMo4 particles are 20.92 μm and 28.42 μm in our experiments (Fig. 1), indicating it is possible to form continuous and even layer thickness.

Overall, the most efficient and reliable method for reducing LoF pores in the LPBF of 42CrMo4 is to improve laser power. Although energy density is not closely related to

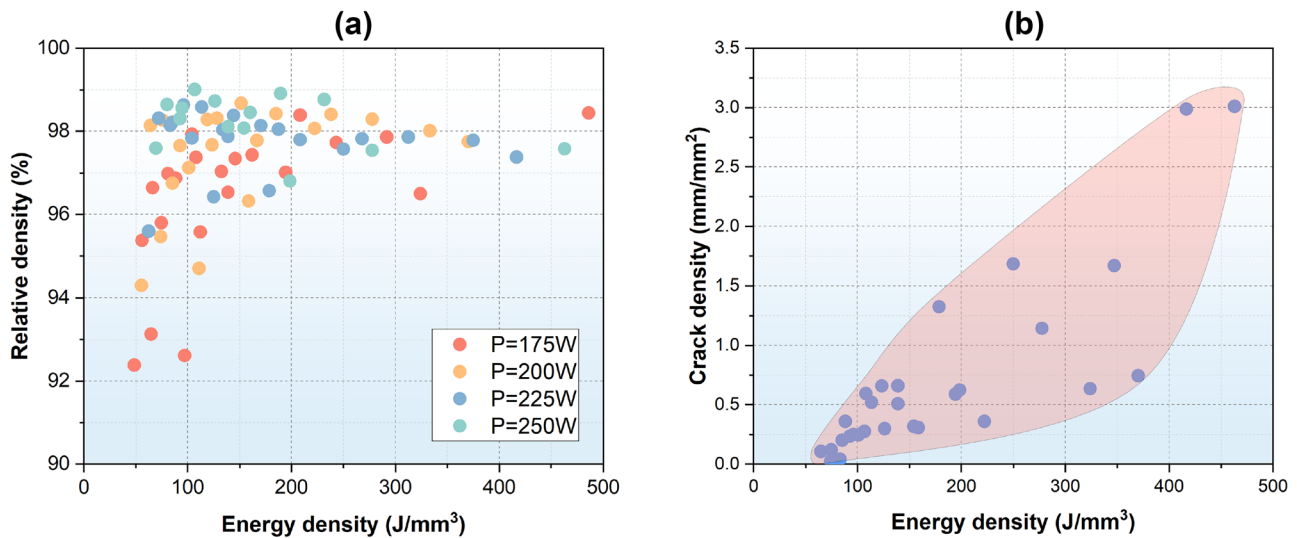


Fig. 8 (a) The relationship between volumetric energy density and relative density and (b) the relationship between energy density and crack density. It shows a nearly linear increase of crack density with increasing energy density

relative density, crack density is susceptible to high energy density. In other words, the crack density increases with increasing energy density (as shown in Fig. 8b). Consequently, high laser power with high scanning speed is the optimized choice to get high relative density and low crack density in LPBF of 42CrMo4.

4.2 Influence of manufacturing size on defects

It is worth noting that although the specimen was manufactured using the same parameters as the small cylindrical samples used for optimizing processing parameters, the relative density dropped by about 1.7%. The variation of relative density, crack density, and microhardness of all three different sizes of specimens are shown in Fig. 9. It was found that the relative density tends to decrease with

increasing the height and areas of specimens, and the dropping trend is extremely prominent in AB specimens. However, the relative density of different sizes could be acceptable for specimens with a base preheating process. The crack density of AB specimens increases with increasing the size (Fig. 9b). However, the crack density of P + AB specimens is stable under 0.01% even with an increase in the size, and it can be ascribed to the reduction in temperature gradient by preheating, which reduced the residual stress. Moreover, the increase in size can reduce the microhardness in AB specimens (Fig. 9c), which can be attributed to the intrinsic tempering effect due to heat accumulation in fabricating large-sized specimens. However, this tempering effect can be ignored as the microhardness values were in a reasonable deviation range.

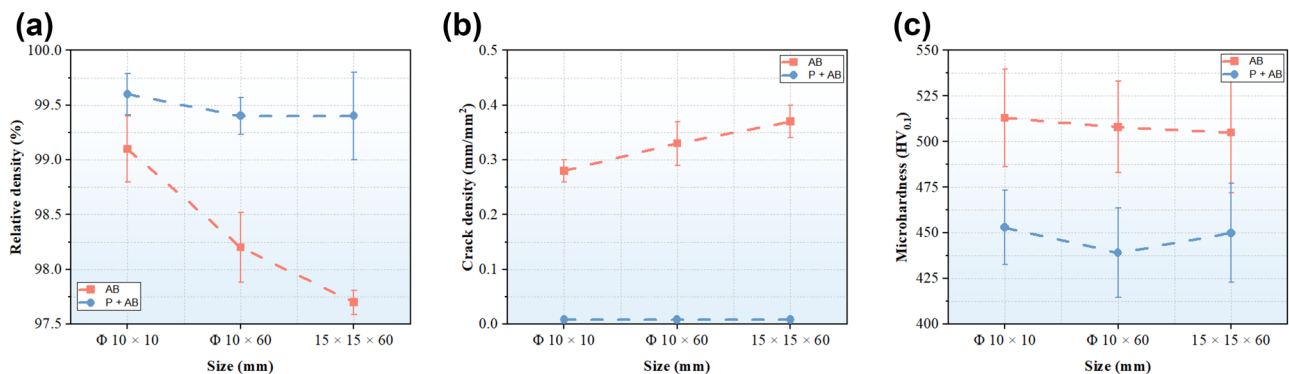


Fig. 9 The influence of manufacturing size with and without preheating on (a) relative density, (b) crack density, and (c) microhardness. P = 250 W, V = 1300 mm/s, and H = 60 μm

Mohr et al. [30] ascribed such height or size effect to keyhole porosity caused by the increase of melt pool depth due to heat accumulation in studying LPBF 316L stainless steel. Nevertheless, keyhole pores may not be the main reason for the sharp drop in relative density of AB specimens. Our results show main keyhole pores (0.6%) in the P+AB specimen, but it is severe LoF pores (2.3%) and some microcracks in the AB specimen in Fig. 10a,c. Nezhadfar et al. [31] proved that preheating could lead to a deeper melt pool than the process without preheating in their experimental work in studying 316L steels manufactured by LPBF. Combining a deeper melt pool and reduced cooling rate by the preheating may reduce the chance of forming LoF defects when simultaneously using the optimized processing parameters in manufacturing large-sized specimens. However, the temperature in the melt pool could be increased due to poor thermal conduction from the melt pool to the build platform by increasing the height, which is full of powders, and the high ambient temperature in the chamber with preheating may help form deeper melt pool to trigger keyhole pores in large-size specimens, and that may be the reason why keyhole pores were seen in P+AB specimens (15 × 15 × 60 mm).

The possible explanation for AB specimens is that the probability of forming LoF increases with increasing the size of the specimen because of occasional spatter droplets. Moreover, the increase in size also means the required time

for manufacturing is extended. Thus, the rubber recoater may be worn during the repeat process and cause the variation in powder layer thickness, thereby inducing LoF pores. Additionally, the long scanning track is susceptible to balling effect when increasing the manufacturing area, which may further increase LoF pores [22].

In summary, LoF pores and crack density will be increased when increasing the manufacturing size, which can be attributed to spatter, wear of recoater and balling caused by long scanning track, and a larger temperature gradient than small specimens. Preheating is a choice to make the optimized processing parameters more repeatable in manufacturing large-scale specimens than without.

4.3 Influence of defects on mechanical performances

4.3.1 Charpy impact toughness

As shown in Fig. 10, there are many LoF pores in the vicinity of the fractured surface sides (Fig. 10a), and these LoF pores can serve as quick paths for crack propagation because of the high-stress concentration near the tips of LoF pores [32]. The low impact energy of AB specimens can be explained by the existence of LoF pores that ease the propagation of cracks (red arrows in Fig. 10a). It also can be verified from

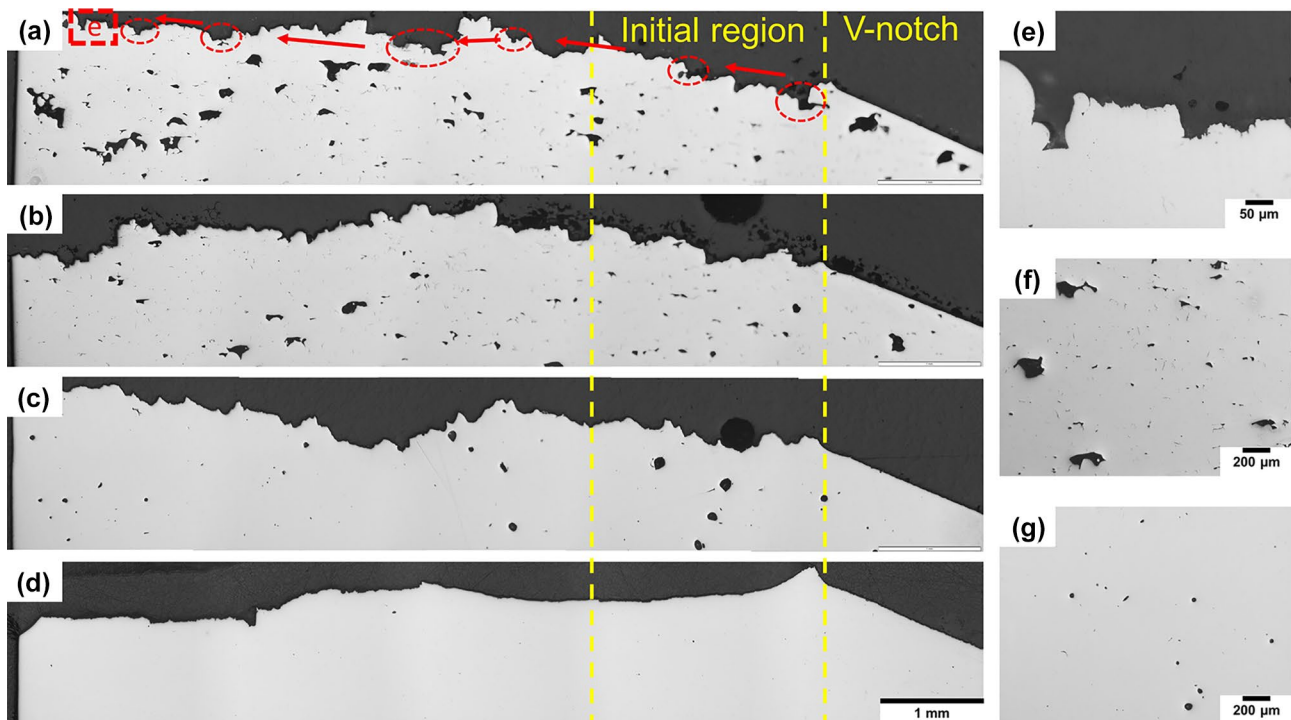


Fig. 10 Optical images of fractured surfaces after Charpy impact test; (a) AB specimen, (b) AB+T450, (c) P+AB, (d) CM+QT450, (e) the magnification of the fractured area in (a), (f) the morphology of

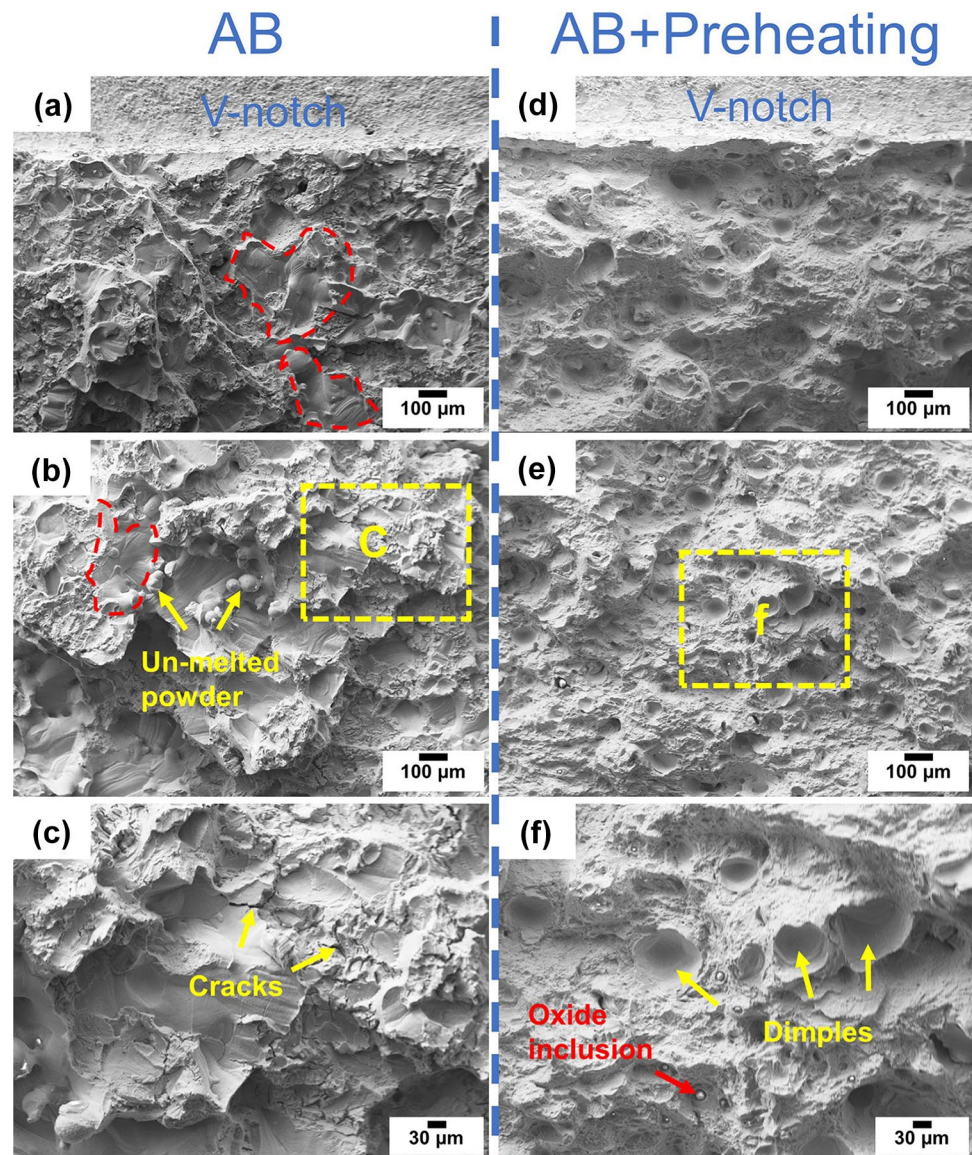
the middle part of the fractured AB specimen, and (g) the morphology of the middle part of the fractured P+AB specimen

SEM figures of the fractured surface. As shown in Fig. 11, the initial region near the V-notch and the middle region of the fractured surface exhibits many relatively smooth small, fractured surfaces (red dotted areas) with unmelted powder (around 55 μm) on them. Based on the morphology feature of the broken surface in Fig. 11a–c, the fracture mode can be categorized as a brittle fracture.

Additionally, small secondary microcracks in the AB specimen can offer multiple paths for crack propagation (Fig. 10f and Fig. 11c). Literature [11, 33] shows the more corrugated fracture surfaces, the better the impact toughness due to crack deflection and respecting energy exhaustion. However, it shows an inverse trend in this study. One explanation is that the jagged shape of the AB specimen was caused by the broken LoF pores or pre-existing cracks (Fig. 10e), as it was the easiest and fastest path for cracks to propagate during the sudden impact.

In contrast, pores in the P + AB specimen are only regular spherical or ellipsoidal keyhole pores (Fig. 10c), so the degree of stress concentration is much lower than in the former. The porosity (0.6%) is also much lower than the AB specimen (2.3%), and there are no apparent cracks in the P + AB microstructure (Fig. 10g). However, the P + AB fractured surface morphology is different from the AB specimen. There are plenty of dimples of about 60.6 μm distributed on the fractured surface, indicating the fracture mode is a ductile fracture, and similar features have also been observed in [34–36]. The plastic deformation during the impact process can absorb more energy than that without dimples. So, the combination of low porosity, no obvious cracks, and low hardness leads to ductile fracture, leading to higher impact absorbed energy for specimens with preheating than those without preheating. Although the post heat treatment for AB specimens can soften the microhardness from 505 to 353

Fig. 11 SEM images of fractured surfaces for LPBF specimens; (a) the fractured surface near the V-notch of the AB specimen, (b) the middle part of the fractured surface of the AB specimen, (c) further magnification of the c area in (b), (d) the fractured surface near the V-notch of the P + AB specimen, (e) the middle part of the fractured surface of the P + AB specimen, and (f) magnification of the f area in (e)



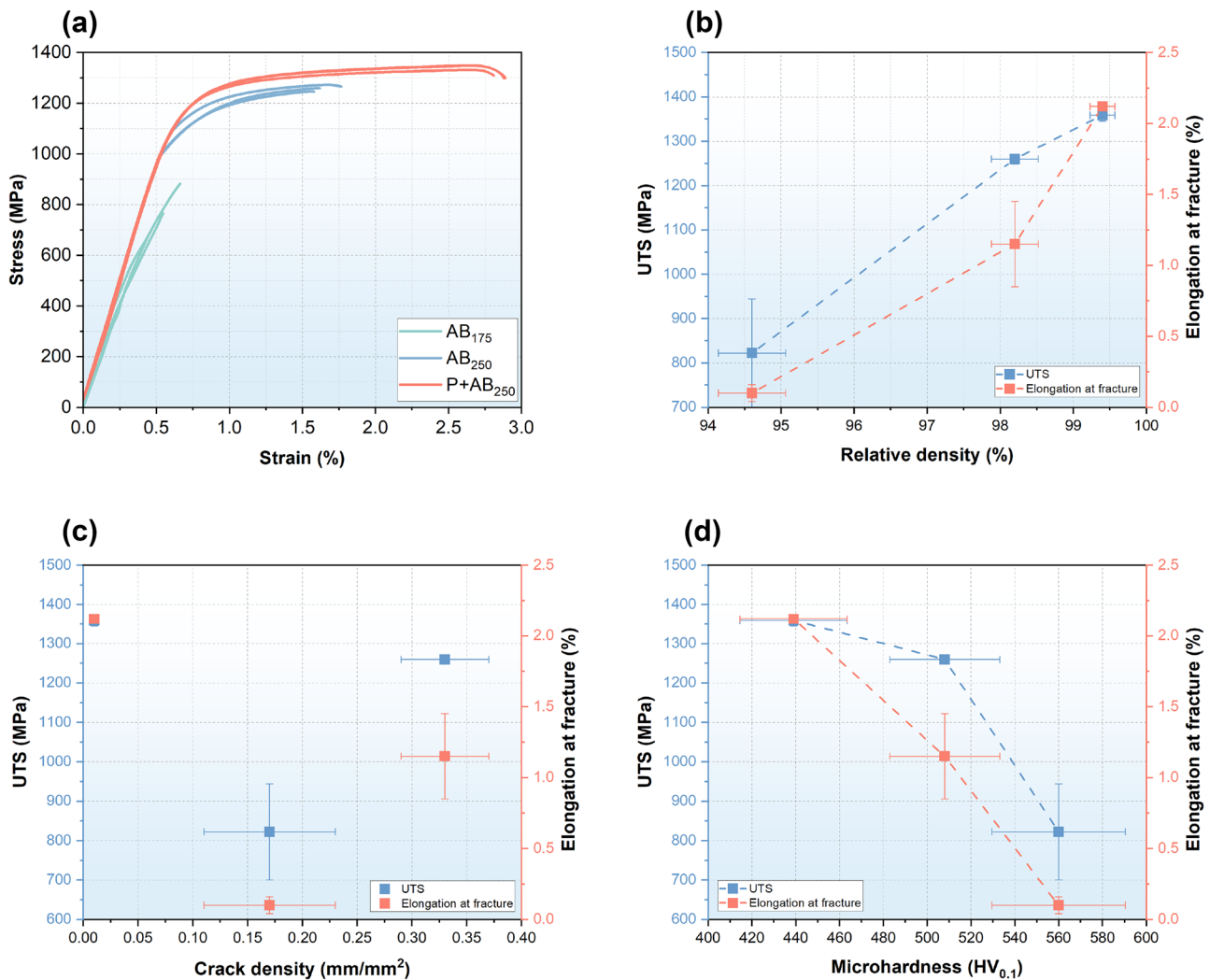


Fig. 12 Tensile results of the LPBF specimens manufactured with different conditions; (a) strain–stress curves, (b) influence of relative density on UTS and A_f , (c) influence of crack density on UTS and A_f , and (d) influence of microhardness on UTS and A_f

$HV_{0.1}$, which can also be seen as a sign of residual stress reduction, the impact energy does not improve any. The reason for the result still can be ascribed to LoF pores and microcracks because the post tempering process does not change the porosity of the specimen (about 2.1–2.4%) or the shapes of pores, and LoF pores and microcracks are still the dominant defects in the microstructure (Fig. 10b).

Due to the fact that the impact toughness is sensitive to porosity, as shown in Fig. 7c, the impact energy dropped sharply with increasing the porosity from 0 to 2%, but there are still some keyhole pores in specimens. Meanwhile, many oxide inclusions [36] are found on the fractured surface of P + AB specimens (Fig. 11f), which indicates a drop in bonding strength and possible initial cracking areas. All the above reasons explain why the impact energy of the P + AB specimen is only 50% of that of the CM specimen. One more thing which should be noted is the impact energy keeps at

low values (around 5 J) and does not fluctuate much when the porosity is over 2%. Hence, reducing pores is a good method to improve the impact toughness prominently.

4.3.2 Tensile strength

Similar to Charpy toughness results, LoF defects with unmelted particles and microcracks in the specimen can lead to premature failure, even at the elastic range stage (Fig. 12). The tensile strength was improved by over 50% when increasing the power laser from 175 to 250 W, and it can be attributed to the reduction of LoF pores, as discussed before. Base preheating further hinders cracking during martensite transformation in the specimen, reducing microcracks in the microstructure. Accordingly, specimens fabricated with preheating have the highest tensile strength.

Although the elongation at fracture (A_f) of the P + AB specimen is more than that of the AB specimen, it is still lower than the A_f values from other researchers. As shown in Fig. 12b–d, A_f is mainly affected by relative density and microhardness. The reasonable explanation could be inferior relative density (99.4%) in this paper to the literature (over 99.5%) and oxide inclusions in the microstructure. It is well known that high hardness can lead to high strength, but it shows that UTS reduces with improving the hardness in Fig. 12d. It can be explained that the intrinsic tempering effect is small when the laser power is 175 W, and the hardness will soften with increasing laser power or by adding preheating to strengthen the tempering effect. Although the crack density is small in the AB₁₇₅ specimen, the large LoF pores caused by insufficient energy at a high scanning speed deteriorate the plasticity and strength, leading to low UTS and A_f at high microhardness value. It again proves that LoF is more detrimental than cracks and keyhole pores.

To sum up, preheating reduces microcracks susceptibility by dropping the temperature gradient. LoF pores and pre-existing microcracks lead the AB specimen to premature failure in the Charpy impact and tensile tests. The feature of samples fabricated with the preheating process displays a slight ductile fracture, but it is just a brittle fracture without preheating.

5 Conclusion

In the present work, 42CrMo4 low alloy steel specimens were successfully manufactured by the LPBF process. Processing parameters, Charpy impact toughness, tensile strength, as well as microhardness of samples under different manufacturing or post-treatment conditions were investigated. The main conclusions are drawn as follows.

- 1) Laser power has a more prominent influence on LoF pores than laser scanning speed and hatch distance. LoF pores will be reduced sharply when increasing the laser power.
- 2) The crack density is closely related to volumetric energy density. Low energy density leads to low crack density, and high energy density leads to severe cracks. High laser power with fast scanning speed is the best choice for improving relative density and reducing cracks simultaneously.
- 3) The impact toughness is sensitive to porosity, especially LoF pores, and the impact energy drops sharply with

increasing the porosity. However, the impact energy will keep at similarly low values when the porosity is over 2%. The P + AB specimens' value is about 3 times more than that for AB specimens. The fracture mode for P + AB specimens is a ductile fracture, which can be attributed to the low LoF porosity and no obvious microcracks. Severe LoF pores and the existence of microcracks, and high hardness are reasons for the brittle fracture of AB specimens.

- 4) The P + AB specimen has the highest tensile strength, which is about 100 MPa more than without preheating. The reason can be ascribed to higher relative density and no LoF pores and microcracks. It also proves that LoF is more detrimental to impact toughness and tensile strength than cracks and keyhole pores.
- 5) Specimens with high relative density and low crack density can be achieved by just optimizing processing parameters in manufacturing small specimens. However, preheating can make the optimized processing parameters repeatable by avoiding possible LoF defects, while the relative density will drop without preheating when manufacturing large specimens.

Supplementary information The online version contains supplementary material available at <https://doi.org/10.1007/s00170-022-09474-9>.

Author contribution Chuan Shi: investigation, writing—original draft. Stefan Dietrich: methodology, writing—review and editing. Volker Schulze: supervision, writing—review and editing.

Funding Open Access funding enabled and organized by Projekt DEAL. This work is financially supported by the program of the China Scholarships Council (No. 201908320344).

Availability of data and material The data that support the findings of this study are available from the corresponding author upon reasonable request.

Code availability Not applicable.

Declarations

Ethics approval Not applicable.

Consent to participate The authors give their consent for participation in this journal.

Consent for publication The authors give their consent for participation in this journal.

Conflict of interest The authors declare no competing interests.

Open Access This article is licensed under a Creative Commons Attribution 4.0 International License, which permits use, sharing, adaptation, distribution and reproduction in any medium or format, as long as you give appropriate credit to the original author(s) and the source, provide a link to the Creative Commons licence, and indicate if changes were made. The images or other third party material in this article are included in the article's Creative Commons licence, unless indicated otherwise in a credit line to the material. If material is not included in the article's Creative Commons licence and your intended use is not permitted by statutory regulation or exceeds the permitted use, you will need to obtain permission directly from the copyright holder. To view a copy of this licence, visit <http://creativecommons.org/licenses/by/4.0/>.

References

- Bajaj P, Hariharan A, Kini A, Kürnsteiner P, Raabe D, Jägler EA (2020) Steels in additive manufacturing: a review of their microstructure and properties. *Mater Sci Eng A* 772:138633. <https://doi.org/10.1016/j.msea.2019.138633>
- Fayazfar H, Salarian M, Rogalsky A, Sarker D, Russo P, Paserin V, Toyserkani E (2018) A critical review of powder-based additive manufacturing of ferrous alloys: process parameters, microstructure and mechanical properties. *Mater Des* 144:98–128. <https://doi.org/10.1016/j.matdes.2018.02.018>
- Damon J, Koch R, Kaiser D, Graf G, Dietrich S, Schulze V (2019) Process development and impact of intrinsic heat treatment on the mechanical performance of selective laser melted AISI 4140. *Addit Manuf* 28:275–284. <https://doi.org/10.1016/j.addma.2019.05.012>
- Kumar P, Ramamurthy U (2020) High cycle fatigue in selective laser melted Ti-6Al-4V. *Acta Mater* 194:305–320. <https://doi.org/10.1016/j.actamat.2020.05.041>
- Wang W, Kelly S (2016) A metallurgical evaluation of the powder-bed laser additive manufactured 4140 steel material. *Jom* 68:869–875. <https://doi.org/10.1007/s11837-015-1804-y>
- Jelis E, Clemente M, Kerwien S, Ravindra NM, Hespos MR (2015) Metallurgical and mechanical evaluation of 4340 steel produced by direct metal laser sintering. *Jom* 67:582–589. <https://doi.org/10.1007/s11837-014-1273-8>
- Taha MA, Yousef AF, Gany KA, Sabour HA (2012) On selective laser melting of ultra high carbon steel: effect of scan speed and post heat treatment. *Materwiss Werksttech* 43:913–923. <https://doi.org/10.1002/mawe.201200030>
- Krell J, Röttger A, Geenen K, Theisen W (2018) General investigations on processing tool steel X40CrMoV5-1 with selective laser melting. *J Mater Process Technol* 255:679–688. <https://doi.org/10.1016/j.jmatprotec.2018.01.012>
- Åsberg M, Fredriksson G, Hatami S, Fredriksson W, Krakhmalev P (2019) Influence of post treatment on microstructure, porosity and mechanical properties of additive manufactured H13 tool steel. *Mater Sci Eng A* 742:584–589. <https://doi.org/10.1016/j.msea.2018.08.046>
- Deirmina F, Peghini N, AlMangour B, Grzesiak D, Pellizzari M (2019) Heat treatment and properties of a hot work tool steel fabricated by additive manufacturing. *Mater Sci Eng A* 753:109–121. <https://doi.org/10.1016/j.msea.2019.03.027>
- Kim H, Park J, Kang M, Lee S (2016) Interpretation of Charpy impact energy characteristics by microstructural evolution of dynamically compressed specimens in three tempered martensitic steels. *Mater Sci Eng A* 649:57–67. <https://doi.org/10.1016/j.msea.2015.09.099>
- Buirette C, Huez J, Gey N, Vassel A, Andrieu E (2014) Study of crack propagation mechanisms during Charpy impact toughness tests on both equiaxed and lamellar microstructures of Ti-6Al-4V titanium alloy. *Mater Sci Eng A* 618:546–557. <https://doi.org/10.1016/j.msea.2014.09.048>
- Chen QY, Chen J, Ren JK, Wang ZH, Liu ZY (2020) Effect of Si content on microstructure and cryogenic toughness of heat affected zone of low nickel steel. *Mater Sci Eng A* 771:138621. <https://doi.org/10.1016/j.msea.2019.138621>
- Jo MC, Park J, Sohn SS, Kim S, Oh J, Lee S (2017) Effects of untransformed ferrite on Charpy impact toughness in 1.8-GPa-grade hot-press-forming steel sheets. *Mater Sci Eng A* 707:65–72. <https://doi.org/10.1016/j.msea.2017.09.027>
- Ghosh A, Modak P, Dutta R, Chakrabarti D (2016) Effect of MnS inclusion and crystallographic texture on anisotropy in Charpy impact toughness of low carbon ferritic steel. *Mater Sci Eng A* 654:298–308. <https://doi.org/10.1016/j.msea.2015.12.047>
- Yang XL, Xu YB, Tan XD, Wu D (2014) Influences of crystallography and delamination on anisotropy of Charpy impact toughness in API X100 pipeline steel. *Mater Sci Eng A* 607:53–62. <https://doi.org/10.1016/j.msea.2014.03.121>
- Wang LZ, Wu JJ, Huang XF, Hong XF (2018) SLM-manufactured 30CrMnSiA alloy: mechanical properties and microstructural effects of designed heat treatment. *Opt Laser Technol* 107:89–98. <https://doi.org/10.1016/j.optlastec.2018.05.020>
- Huang B, Zhai Y, Liu S, Mao X (2018) Microstructure anisotropy and its effect on mechanical properties of reduced activation ferritic/martensitic steel fabricated by selective laser melting. *J Nucl Mater* 500:33–41. <https://doi.org/10.1016/j.jnucmat.2017.12.011>
- Fu J, Li H, Song X, Fu MW (2022) Multi-scale defects in powder-based additively manufactured metals and alloys. *J Mater Sci Technol* 122:165–199. <https://doi.org/10.1016/j.jmst.2022.02.015>
- Wang J, Liu S, Fang Y, He Z (2020) A short review on selective laser melting of H13 steel. *Int J Adv Manuf Technol* 108:2453–2466. <https://doi.org/10.1007/s00170-020-05584-4>
- Du Plessis A (2019) Effects of process parameters on porosity in laser powder bed fusion revealed by X-ray tomography. *Addit Manuf* 30:100871. <https://doi.org/10.1016/j.addma.2019.100871>
- Rayleigh L (1878) Lord Rayleigh on the instability of jets. *Proc London Math Soc* 10:4–13
- Zhao C, Parab ND, Li X, Fezzaa K, Tan W, Rollett AD, Sun T (2020) Critical instability at moving keyhole tip generates porosity in laser melting. *Science* 370:1080–1086. <https://doi.org/10.1126/science.abd1587>
- Guo C, Li S, Shi S, Li X, Hu X, Zhu Q, Ward RM (2020) Effect of processing parameters on surface roughness, porosity and cracking of as-built IN738LC parts fabricated by laser powder bed fusion. *J Mater Process Technol* 285:116788. <https://doi.org/10.1016/j.jmatprotec.2020.116788>
- Xia M, Gu D, Yu G, Dai D, Chen H, Shi Q (2016) Influence of hatch spacing on heat and mass transfer, thermodynamics and laser processability during additive manufacturing of Inconel 718 alloy. *Int J Mach Tools Manuf* 109:147–157. <https://doi.org/10.1016/j.ijmactools.2016.07.010>
- Thijs L, Verhaeghe F, Craeghs T, Van HJ, Kruth JP (2010) A study of the microstructural evolution during selective laser melting of Ti-6Al-4V. *Acta Mater* 58:3303–3312. <https://doi.org/10.1016/j.actamat.2010.02.004>
- Kudzal A, McWilliams B, Hofmeister C, Kellogg F, Yu J, Taggart-Scarff J, Liang J (2017) Effect of scan pattern on the microstructure and mechanical properties of Powder Bed Fusion additive manufactured 17–4 stainless steel. *Mater Des* 133:205–215. <https://doi.org/10.1016/j.matdes.2017.07.047>
- Jia H, Sun H, Wang H, Wu Y, Wang H (2021) Scanning strategy in selective laser melting (SLM): a review. *Int J Adv Manuf Technol* 113:2413–2435. <https://doi.org/10.1007/s00170-021-06810-3>

29. Macchi J, Gaudez S, Geandier G, Teixeira J, Denis S, Bonnet F, Allain SYP (2021) Dislocation densities in a low-carbon steel during martensite transformation determined by in situ high energy X-Ray diffraction. *Mater Sci Eng A* 800:140249. <https://doi.org/10.1016/j.msea.2020.140249>
30. Mohr G, Altenburg SJ, Hilgenberg K (2020) Effects of inter layer time and build height on resulting properties of 316L stainless steel processed by laser powder bed fusion. *Addit Manuf* 32:101080. <https://doi.org/10.1016/j.addma.2020.101080>
31. Nezhadfar PD, Shamsaei N, Phan N (2021) Enhancing ductility and fatigue strength of additively manufactured metallic materials by preheating the build platform. *Fatigue Fract Eng Mater Struct* 44:257–270. <https://doi.org/10.1111/ffe.13372>
32. Liu QC, Elambasseril J, Sun SJ, Leary M, Brandt M, Sharp PK (2014) The effect of manufacturing defects on the fatigue behaviour of Ti-6Al-4V specimens fabricated using selective laser melting. *Adv Mater Res* 891–892:1519–1524. <https://doi.org/10.4028/www.scientific.net/AMR.891-892.1519>
33. Chi G, Yi D, Jiang B, Yang L, Liu H (2021) Crack propagation during Charpy impact toughness testing of Ti–Al–V–Mo–Zr alloy tubes containing equiaxed and lamellar microstructures. *J Alloys Compd* 852:156581. <https://doi.org/10.1016/j.jallcom.2020.156581>
34. Kumar P, Jayaraj R, Suryawanshi J, Satwik UR, McKinnell J, Ramamurty U (2020) Fatigue strength of additively manufactured 316L austenitic stainless steel. *Acta Mater* 199:225–239. <https://doi.org/10.1016/j.actamat.2020.08.033>
35. Mitra A, Mohapatra JN, Swaminathan J, Ghosh M, Panda AK, Ghosh RN (2007) Magnetic evaluation of creep in modified 9Cr-1Mo steel. *Scr Mater* 57:813–816. <https://doi.org/10.1016/j.scriptamat.2007.07.004>
36. Kim H, Liu Z, Cong W, Zhang HC (2017) Tensile fracture behavior and failure mechanism of additively-manufactured AISI 4140 low alloy steel by laser engineered net shaping. *Materials* 10:1283. <https://doi.org/10.3390/ma10111283>

Publisher's Note Springer Nature remains neutral with regard to jurisdictional claims in published maps and institutional affiliations.